

Optical Switching Through Graphene-Induced Exceptional Points

DIMITRIOS CHATZIDIMITRIOU^{1*} AND EMMANOUIL E. KRIEZIS¹

¹School of Electrical and Computer Engineering, Aristotle University of Thessaloniki, Thessaloniki GR-54124, Greece

*dchatzid@ece.auth.gr

Compiled May 4, 2018

The switching properties of coupled nanophotonic waveguides under the influence of a loss induced exceptional point are analytically and numerically investigated. The specific requirements for switching/routing functionality are determined and an analytically predicted lower boundary for the insertion losses is established. These passive PT-Symmetric dynamics are substantiated in a silicon photonic coupler through the use of graphene layers. Graphene's chemical potential is properly tuned, in accordance with the exceptional point requirements, for the electro-optic control of its surface conductivity. All analytically derived findings are numerically verified enabling linear, low-loss, and high extinction ratio switching elements. Finally, a polarization dependent photonic switch is proposed based on both exceptional points and graphene's anisotropic surface conductivity. © 2018 Optical Society of America

OCIS codes: (130.4815) Optical switching devices, (250.5300) Photonic integrated circuits, (130.3130) Integrated optics materials, (260.3090) Infrared, far.

<http://dx.doi.org/10.1364/ao.XX.XXXXXX>

1. INTRODUCTION

Exceptional points (EPs) constitute singularities in functions describing observable physical quantities and are generally encountered in eigenvalue problems that are dependent on a parameter [1]. At these critical values in the parameter space the eigenvalues coalesce, drastically altering the behaviour of the physical system [2, 3]. In photonic systems the most notable application of EPs is the Parity-Time Symmetry (PT-Symmetry) concept [4] which involves two coupled photonic elements with balanced gain and loss so that the refractive index profile obeys the relation [5] $n(x) = n^*(-x)$, ($*$) denoting complex conjugation.

PT-Symmetric photonic systems, where the eigenvalues coalesce for a specific value of the gain/loss parameter, have generated intense theoretical and experimental research since their first experimental demonstration [6]. Specifically, a diverse range of functionalities under PT symmetry conditions have been investigated: e.g. switching/modulation [7–10], spatial modal selectivity [11], single-mode lasing [12], unidirectional propagation/invisibility [13, 14], mode conversion [15] and non-reciprocal transmission [16]. Even though such systems exhibit very intriguing behaviour, the requirement of gain in integrated photonic components, especially in silicon based devices, complicates the manufacturing process.

In this work we investigate the routing/switching of light in linear and purely lossy photonic devices operating in the vicinity

of an EP. Such systems are not strictly PT-Symmetric due to the absence of balanced gain and loss, nevertheless the existence of the EP in passive photonic systems has been dubbed as “Passive PT-Symmetry” [17]. The critical parameters of extinction ratio (ER) and insertion losses (IL) are assessed in this class of devices and the existence of a minimum IL level inherent to the material used for the loss modulation is revealed both through analytic relations and simulation. The analytic expressions deduced are general and valid for any material choice. Graphene is employed as a means of modulating the losses of one of the coupler's arms, a choice based on graphene's tunable (by means of externally applied bias-voltage) electric conductivity [18, 19]. Utilising typical silicon-photonic couplers enhanced by graphene it is shown that the proposed devices can operate as 1×2 switches with very moderate IL (in the range of a couple of dBs), high ER and compact lengths (tens of micrometers). The operation described is an entirely linear process and additionally does not involve resonant structures enabling low power and broadband application. Finally, graphene's anisotropic surface conductivity [20] is exploited so as to differentiate TE and TM polarizations with respect to operation above or below of an EP and thus exhibit polarization dependent switching.

This paper is organised into three sections. In the first section the impact of an EP on the super-modes (eigenvalues) of a lossy (non-Hermitian) photonic coupler is discussed and the principles and requirements for its linear operation as a photonic router are analytically derived. Furthermore, it is established

that such a passive system exhibits a minimum level of IL. In the second section, graphene properties are presented, namely its tunable electric surface conductivity, and proper biasing conditions for passive PT-Symmetric operation are investigated. In the last section, transmission characteristics of the passive PT-Symmetric switch and polarization dependent switch are assessed.

2. PASSIVE PT-SYMMETRY

In this section we present fundamental concepts regarding the operation of a non-Hermitian coupler and perform an analytical investigation of its switching capabilities based on the existence of exceptional points in the loss coefficient parameter space.

A. Impact and existence of an exceptional point

We start by considering two lossy single-mode waveguides and assume that the supported modes' complex propagation constants are given by $\beta_1 - j\alpha_1$ and $\beta_2 - j\alpha_2$, corresponding to the first and second waveguide, respectively. Coupling between two such waveguides is commonly described through the coupled mode theory (CMT) formulation [21, 22]:

$$\frac{\partial}{\partial z} A_1(z) = -j(\beta_1 - j\alpha_1)A_1(z) + \kappa A_2(z), \quad (1a)$$

$$\frac{\partial}{\partial z} A_2(z) = -j(\beta_2 - j\alpha_2)A_2(z) - \kappa^* A_1(z), \quad (1b)$$

where A_1 and A_2 are the complex amplitudes of the modes propagating in the respective waveguides and κ is the coupling coefficient. We assume that modes differ only in their loss coefficients so that $\beta \equiv \beta_1 = \beta_2$ and $\alpha_1 \neq \alpha_2$ with $\alpha_1 \ll \alpha_2$. The eigenvalues of (1) are analytically calculated:

$$\beta_{S,A} = \left[\beta \pm \sqrt{|\kappa|^2 - \left(\frac{\Delta\alpha}{2}\right)^2} \right] - j\frac{\alpha_1 + \alpha_2}{2}, \quad (2)$$

where $\beta_{S,A}$ are the complex propagation constants of the supported symmetric/anti-symmetric super-modes and $\Delta\alpha = \alpha_2 - \alpha_1$. Due to the non-Hermitian nature of the system, inspection of (2) reveals the existence of an EP at $|\Delta\alpha| = 2|\kappa|$. While $|\Delta\alpha| \ll 2|\kappa|$, the system behaves as a conventional lossy photonic coupler with a coupling length of $L_c = \pi/(\beta_S - \beta_A) = \pi/(2|\kappa|)$. On the other hand when $|\Delta\alpha| > 2|\kappa|$ the real part of the eigenvalues shown in (2) coalesce:

$$\beta_{S,A} = \beta - j\left[\frac{\alpha_1 + \alpha_2}{2} \mp \sqrt{\left(\frac{\Delta\alpha}{2}\right)^2 - |\kappa|^2} \right], \quad (3)$$

and as $\Delta\alpha$ grows, they asymptotically evolve into the uncoupled propagation constants $\beta - j\alpha_1$ and $\beta - j\alpha_2$. Since the propagation constants evolve into their uncoupled counterparts, the same behavior should be expected from the respective mode profiles. Thus, in the regime beyond the EP, there exist a high and a low loss super-mode confined into the high and low loss waveguide, respectively. Consequently, regardless of which waveguide is initially excited only the low loss super-mode will survive for sufficiently long propagation distance.

Finally, note that the condition $\beta \equiv \beta_1 = \beta_2$ does not necessarily require that the waveguides be identical, either geometrically or material-wise, it only entails that light effectively experiences them in the same way. This observation implies that, in classic photonic PT-Symmetric systems for example, the

requirement of $n(x) = n^*(-x)$ can be generalised as $\beta_1 = \beta_2^*$. In this work we still consider two identical waveguides, but utilising the relaxed condition could lead to a broader application of PT-Symmetry.

B. Analytic investigation

The dynamics of passive PT-Symmetry described in Section A can be exploited for the routing of light: a cross state for operation below the EP and a bar state above the EP. We start by setting the coupler length equal to L_c and assuming first that $\alpha_1 \equiv 0$ so that $\Delta\alpha = \alpha_2$, and secondly that we are able to vary α_2 between a low and high value, $\alpha_L \leq \alpha_2 \leq \alpha_H$.

The cross state is straight forward to realise and is based on conventional photonic coupler operation: α_2 is set to $\alpha_L < 2|\kappa|$ so that light is normally coupled from one waveguide to the other. If we assume that guided power at length z in waveguide 1 or 2 is given by $|A_{1,2}(z)|^2$ then power losses at $z = L_c$ can be estimated from (2) and are equal to

$$T_{\text{cross}} = 10 \log_{10} \left(\frac{|A_{1,2}(L_c)|^2}{|A_{2,1}(0)|^2} \right) = -4.343\alpha_L L_c, \quad (4)$$

where we ignored the de-tuning of the coupler due to losses. This kind of operation is widely known and has been extensively studied over the years [23].

The bar state is realised through operation above the EP. We set $\alpha_2 = \alpha_H > 2|\kappa|$ with the corresponding super-mode propagation constants given by (3). The analytical solution of (1) involves exponential terms of both super-modes, therefore by ignoring the high loss components the solution can be approximately written as:

$$\begin{bmatrix} A_1(z) \\ A_2(z) \end{bmatrix} = \begin{bmatrix} \frac{\alpha_H/2 + \beta_0}{2\beta_0} & \frac{\kappa}{2\beta_0} \\ -\frac{\kappa^*}{2\beta_0} & -\frac{\alpha_H/2 - \beta_0}{2\beta_0} \end{bmatrix} \begin{bmatrix} A_1(0) \\ A_2(0) \end{bmatrix} \times e^{-(\alpha_H/2 - \beta_0)z} e^{-j\beta z}, \quad (5)$$

where $\beta_0 = \sqrt{(\alpha_H/2)^2 - |\kappa|^2}$. Several useful conclusions can be drawn from (5): Firstly, power output is always greater from the lossless waveguide. This is easily verified since the relations

$$\begin{aligned} \frac{\alpha_H/2 + \beta_0}{2\beta_0} &> \frac{|\kappa|}{2\beta_0} \quad \text{for} \quad \begin{bmatrix} A_1(0) \\ A_2(0) \end{bmatrix} = \begin{bmatrix} 1 \\ 0 \end{bmatrix}, \\ \frac{|\kappa|}{2\beta_0} &> \frac{\alpha_H/2 - \beta_0}{2\beta_0} \quad \text{for} \quad \begin{bmatrix} A_1(0) \\ A_2(0) \end{bmatrix} = \begin{bmatrix} 0 \\ 1 \end{bmatrix}, \end{aligned} \quad (6)$$

always hold above the EP. Hence, a bar state is feasible for injection of light into the lossless waveguide. In this case, power losses are given by:

$$\begin{aligned} T_{\text{bar}} &= 10 \log_{10} \left(\frac{|A_1(L_c)|^2}{|A_1(0)|^2} \right) = \\ &= -4.343 \left[\alpha_H L_c - \sqrt{(\alpha_H L_c)^2 - \pi^2} \right]. \end{aligned} \quad (7)$$

Note that in defining losses through (7) the multiplicative term of (5) is intentionally omitted due to its limited importance (approximately equal to 1) for sufficiently high α_H and also for

the purpose of simplifying the expression. Inspecting (7) it is straightforward to show that T_{bar} goes to zero in the limit of $\alpha_H \rightarrow \infty$, implying that the higher loss coefficient α_H that can be achieved, the lower the propagation losses in this regime. Additionally, when considering power output, diagonal elements of (5) are not equal whereas the off-diagonal elements are identical in magnitude. Therefore transmission is asymmetric but still reciprocal. The latter underlines that the existence of an EP alone is not enough to break reciprocity, a fact which was also experimentally verified for two PT-Symmetric ring resonators [16]. Finally, in the limit of $\alpha_H \rightarrow \infty$, (5) takes the form of:

$$\begin{bmatrix} A_1(z) \\ A_2(z) \end{bmatrix} = \begin{bmatrix} 1 & 0 \\ 0 & 0 \end{bmatrix} \begin{bmatrix} A_1(0) \\ A_2(0) \end{bmatrix} e^{-j\beta z}. \quad (8)$$

Thus, because (7) and (8) suggest that α_H is required to be high for losses in this state to be low, it is not possible to use the lossy waveguide for light injection ($[A_1(0), A_2(0)] = [0, 1]$), as it would result in very poor transmission. Similar analytic results for active PT-Symmetry were also shown in [24].

To summarize, the routing/switching dynamic for a coupler of length L_c is composed of a cross state for operation below the EP ($\alpha_2 = \alpha_L$) and normalized power losses equal to T_{cross} of (4), whereas the bar state is identified for operation above the EP ($\alpha_2 = \alpha_H$) with approximate power losses equal to T_{bar} of (7). In both states, only the lossless waveguide is initially excited.

Finally, inspecting the expressions for the output losses in (4) and (7) we observe that for constant values of α_H and α_L , T_{cross} is a decreasing function of L_c whereas T_{bar} is an increasing function of L_c . Therefore, if we set $T_{\text{av}} = (T_{\text{cross}} + T_{\text{bar}})/2$, then there exists a maximum of T_{av} , calculated as $\partial T_{\text{av}}/\partial L_c = 0$. We clarify that the maximum of T_{av} , e.g. maximum transmission, is referred to as a minimum when addressing IL. Solving the equation results in:

$$\tilde{L}_c = \frac{\pi}{\alpha_H} \frac{1 + \alpha_L/\alpha_H}{\sqrt{(\alpha_L/\alpha_H)^2 + 2\alpha_L/\alpha_H}}, \quad (9a)$$

$$\max\{T_{\text{av}}\} = -0.5\pi \sqrt{(\alpha_L/\alpha_H)^2 + 2\alpha_L/\alpha_H}. \quad (9b)$$

Note that $\max\{T_{\text{av}}\}$ is a function of α_L/α_H . The implications of this are tied to the material used and will be discussed in the following section.

3. LOSS MODULATION WITH GRAPHENE

In the previous section, the analysis was based solely on the mathematical model of the CMT equations without any reference to material properties that could realise the underlying physics of EPs. In this section we employ monolayer graphene and few layer graphene (FLG) as a means to modulate losses of one of the waveguides in a silicon photonic coupler and tune the coupler's operation below or above the EP.

The photonic coupler consists of two air-clad silicon ($n_{\text{Si}} = 3.45$) strip waveguides, 320 nm wide and 280 nm thick, on top of a silicon oxide ($n_{\text{SiO}_2} = 1.48$) substrate. The waveguides are separated by a 440 nm wide gap, which sets $L_c \simeq 39.7 \mu\text{m}$ for the first TE mode at the free space telecom wavelength $\lambda_0 = 1.55 \mu\text{m}$. A stack of two graphene monolayers (or FLG sheets) with a 7 nm layer of Al_2O_3 ($n_{\text{Al}_2\text{O}_3} = 1.66$) in between is used to coat one of the waveguides, whilst the other is only coated by alumina, also of 7 nm thickness. The complete layout can be seen in

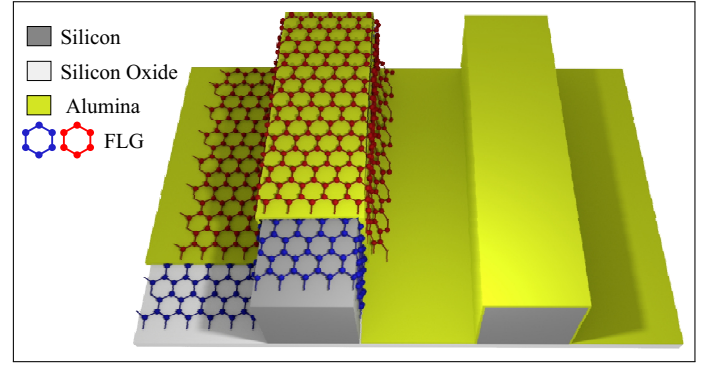


Fig. 1. Schematic of a photonic coupler enhanced by a graphene/alumina/graphene stack. The coupler consists of two silicon strip waveguides on a silicon oxide substrate. The left waveguide is coated with graphene/alumina/graphene whilst the right waveguide only retains the alumina coating.

Fig. 1. The loss modulation of the graphene coated waveguide is theoretically investigated using a finite element method (FEM) formulation for the eigenmode analysis of the waveguide's cross-section.

A. Graphene's Surface Conductivity

Graphene's surface conductivity can be tuned by changing its chemical potential μ_c , a quantity that in graphene coincides with the Fermi level. Additionally, the chemical potential can be dynamically altered through external electrostatic biasing of the graphene/alumina/graphene stack, which forms a capacitor-like structure. Specifically, the applied voltage induces (opposite) surface charge densities on the graphene sheets which in turn alter the chemical potential. If graphene sheets are thought to be undoped then we can relate the chemical potential to the applied voltage V_{bias} through the relation [25, 26]:

$$V_{\text{bias}} = \frac{\mu_c^2}{\pi\eta\hbar^2 v_F^2} \quad (10)$$

where $v_F = c_0/300$ is the Fermi velocity, c_0 is the speed of light in vacuum and $\eta = (\epsilon_0\epsilon_d)/(et_d)$ is a parameter extracted from the capacitor model. In the latter parameter, ϵ_0 is the vacuum permittivity, ϵ_d is the low frequency relative permittivity of alumina, e is the electron charge and t_d is the dielectric thickness. For the case of the stack used $\eta = 9 \times 10^{16} (\text{m}^2\text{V})^{-1}$. Note that unlike pn-junctions where there is a linear dependence of V_{bias} to the local quasi-Fermi levels, here the Fermi level (chemical potential) μ_c has a square root dependence to V_{bias} . This is because in graphene the chemical potential is proportional to the square root of the surface charge density n ($\mu_c \propto \sqrt{n}$) and the latter is linearly dependent to the bias voltage ($n \propto V_{\text{bias}}$), as dictated by a simple capacitor model. Such behavior is attributed to graphene's linear dispersion and massless Dirac fermions [27].

For μ_c greater than half the photon energy ($\hbar\omega$), interband electron transitions are prohibited, due to Pauli blocking, and graphene is rendered almost transparent [28]. The real and imaginary part of graphene's surface conductivity σ are plotted in Fig. 2 for a wide range of chemical potential and photon energy values. Note that since graphene is an atomically thin material it only interacts with electromagnetic radiation tangential to its surface. This inherent anisotropy will be exploited in the last

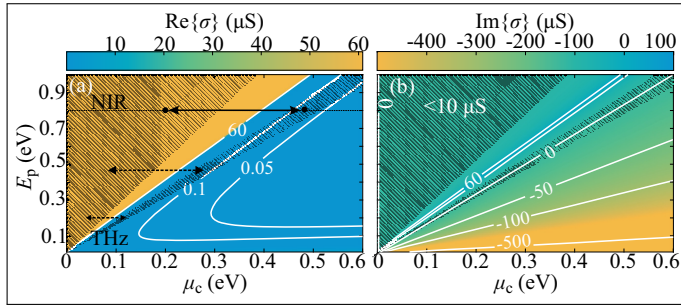


Fig. 2. (a) Real and (b) imaginary part of graphene's surface conductivity σ (in μS) versus chemical potential μ_c and photon energy $E_p = \hbar\omega$. The conductivity was plotted assuming an intraband relaxation time of 40 ps. In (a) there exist two well defined regions of high and low losses on either side of $\mu_c = E_p/2$. In (b) the imaginary part varies in a considerable range depending on E_p and μ_c . The shaded areas correspond to a low ($|\text{Im}\{\sigma\}| < 10 \mu\text{S}$) imaginary part. Arrows show possible pairs of operation points: the solid arrow corresponds to the values used in this work while dashed arrows correspond to lower frequencies.

section to enable polarization dependent switching. Returning to Fig. 2 we first observe the sharp change in the real part of the conductivity (loss level) when $\mu_c > \hbar\omega/2$, and secondly the existence of areas with small to near-zero imaginary part on either side of $\hbar\omega/2$ (which corresponds to 0.4 eV at a wavelength of 1.55 μm). Both of these features are critical for the intended passive PT-Symmetric switching operation as the former ensures a high conductivity difference for a moderate shift of μ_c and the latter, alongside graphene's infinitesimal thickness (0.33 nm), indicates that graphene will have negligible impact on the waveguiding/profiles of the photonic modes. Note that for high photon energies (NIR spectral region), where graphene needs to be biased to the areas of low imaginary conductivity (shaded areas), we can always find two values of the chemical potential that correspond to high/low losses and thus satisfy the PT-Symmetry operation requirements.

As the frequency decreases we observe that the shaded areas in Fig. 2, which mark potential μ_c pairs that lead to low imaginary conductivity, become vanishingly small. This is more pronounced for the shaded area in the low conductivity regime. Even at 50 THz (0.2 eV) biasing to the low loss region [see dashed arrows in 2(a)] must be done with accuracy of 5 meV. Furthermore, contrary to higher frequencies, failing to accurately bias graphene would lead to a significant change in the propagation constant of the mode as the surrounding graph area is characterized by higher (imaginary) conductivity values. We should also comment that it is not possible to apply our passive PT-Symmetry switching scheme to graphene waveguides supporting SPPs, e.g. graphene nano-ribbons [29]. This is due to the fact that in order to support SPP waves, graphene needs to be doped/biased to an area of high negative imaginary conductivity, which according to Fig. 2(b) does not overlap with the high losses area and thus no loss modulation is possible. Finally, note that in this work we only assess passive scenarios, active PT-Symmetry breaking in graphene nano-ribbons [30] is still possible since the tuning of operation above or below the EP can be performed through modulation of the gain, for a constant value of μ_c , alleviating the restrictions presented here. Consequently, we solely focus on operation in the telecom wave-

length where graphene's tunability provides a crucial way to dynamically manipulate the loss level of one of the waveguides, enabling the switching of operation above or below the EP.

B. Loss Coefficients

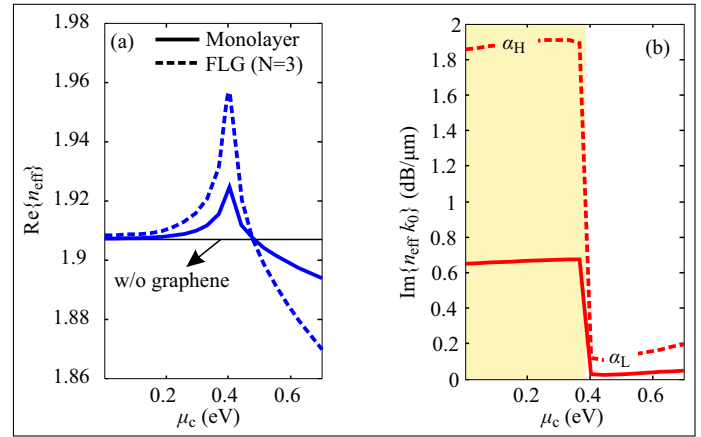


Fig. 3. Evolution of the real (a) and imaginary (b) part of the effective index of the graphene coated waveguide versus graphene's chemical potential when considering monolayer graphene (solid lines) or FLG (dashed lines). A black solid line in (a) denotes the effective index of the waveguide without graphene. Setting μ_c to 0.2 eV and 0.48 eV enables the tuning of the loss coefficient from α_H to α_L , as shown in (b), with minimal deviation from the $\text{Re}\{n_{\text{eff}}\}$ of the waveguide without graphene.

We start by utilizing two graphene monolayers in the graphene/alumina/graphene stack as a means of loss modulation. Considering only the waveguide coated with graphene we plot in Fig. 3 the dependence of the effective refractive index, $n_{\text{eff}} = (\beta - j\alpha_2)/k_0$, of the first TE mode versus graphene's chemical potential. Note that the dependence of n_{eff} on μ_c closely resembles that of graphene's surface conductivity on μ_c (Fig. 2). Below and above the interband transition blocking point we readily identify a high and a low loss region, respectively. On the other hand, in the vicinity of $\mu_c = 0.4$ eV the real part of n_{eff} deviates quite strongly from that of the waveguide without graphene suggesting that caution should be taken for appropriate biasing, lest the system operation be dominated by the de-synchronization of the waveguides. Nevertheless, we can still choose μ_c accordingly, namely at 0.2 eV and ~ 0.48 eV, so that graphene's conductivity only modulates the losses of the guided mode.

Comparing the induced losses (0.32 dB/ μm for $\mu_c = 0.2$ eV) to previously reported designs [31] we underline that a waveguide coated with graphene may yield better/equivalent loss modulation than more complex waveguide structures which try to place graphene close to the maximum of the mode's dominant electric field component (E_x for the TE modes). That is because modes in nanophotonic silicon strip waveguides exhibit strong longitudinal electric field components (E_z) on the outer edges of the silicon area and the overlap of the coated graphene with E_z can counterbalance the small overlap with E_x . To support this argument the TE mode profile is plotted in Fig. 4(a),(b) alongside the tangential electric field norm calculated on the graphene curve in Fig. 4(c).

In terms of the CMT model of Section 2, we calculate

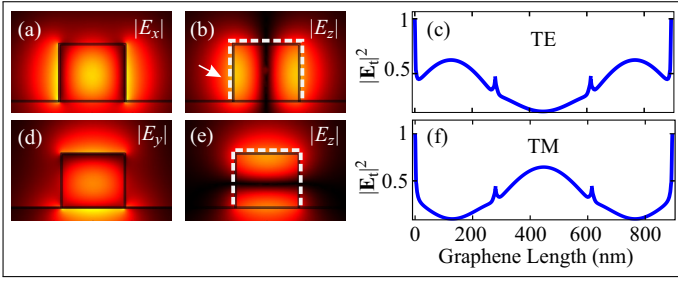


Fig. 4. Field distributions of the norm of the dominant electric field components E_x and E_y along with the longitudinal E_z component of the first TE (a),(b) and TM (d),(e) modes, respectively. A white dashed line highlights the graphene curve on which the norm of the tangential electric field E_t is calculated and depicted in (c),(f) for the respective polarization. The calculation of E_t reveals that both modes exhibit similar overlap with graphene and highlights the importance of the contribution of E_z .

$\alpha_L = \text{Im}\{n_{\text{eff}}k_0\} = 0.04 \text{ dB}/\mu\text{m}$ at $\mu_c = 0.48 \text{ eV}$ and $\alpha_H = 0.64 \text{ dB}/\mu\text{m}$ at $\mu_c = 0.2 \text{ eV}$, where k_0 is the free space wavenumber. For the given set-up, (3) requires that $\alpha_H/2 > |\kappa|$ or equivalently that $L_c > \pi/\alpha_H \simeq 43 \mu\text{m}$ which is higher than the current $L_c = 39.7 \mu\text{m}$ design, demonstrating that the use of graphene monolayers does not provide a high enough loss state to reach the EP. Furthermore, since the system is inherently lossy, just reaching the EP would entail impairing insertion losses; by calculating the optimum coupling length with respect to losses from (9a) yields $\tilde{L}_c = 127 \mu\text{m}$ with $\max\{T_{\text{av}}\} \simeq -2.5 \text{ dB}$. Hence, in order to achieve low loss operation it is imperative to either increase L_c and consequently the length of the coupler or manage to achieve a higher loss state α_H .

To that end, two strategies can be employed, either graphene is integrated in a more optimal way so as to maximize the overlap of the tangential (to the graphene sheets) electric field components [32] or we could employ multiple graphene sheets. The former approach could alleviate the problem but bare in mind that, as it will be shown, we should have to almost triple the current loss coefficients in order to reach the optimal loss point. This is deemed rather hard from a manufacturing point of view, as even the coating of the waveguide with the graphene/alumina/graphene stack is a demanding process. Thus, we follow the second route and instead of using two graphene monolayers we employ two FLG layers which consists of $N = 3$ graphene monolayers each (e.g. two tri-layer graphene sheets).

It should be underlined that FLG optical properties [33–35] and their dependence on electrostatic gating are a non-trivial matter since they are highly dependent on the type of stacking of the graphene layers, the operation frequency, etc. In this work and for the near-infrared spectral region we employ the simplified model of implementing FLG as a stack of N independent (uncoupled) monolayers [36, 37]. Specifically for ABA tri-layer graphene, the optical conductivity was theoretically calculated in [38] showing good qualitative agreement with our approach. Furthermore, very recently the selective fabrication of both ABA and ABC stacked tri-layer graphene was reported in [39]. In conclusion, as far as the linear surface conductivity is concerned, we assume in this work that for $N < 9$ the FLG conductivity is that of a monolayer's multiplied by the number of monolayers N . The same trend is also inherited to the loss coefficients of the

waveguide modes, as shown in Fig. 3.

Renaming the previously calculated loss coefficients for the monolayer case as α_ℓ and α_h , then the loss coefficients for the current FLG case are $\alpha_L \simeq 0.12 \text{ dB}/\mu\text{m}$ and $\alpha_H \simeq 1.92 \text{ dB}/\mu\text{m}$ verifying that $\alpha_L/\alpha_\ell = \alpha_H/\alpha_h \simeq N = 3$. For these new values we calculate $\tilde{L}_c = 42.5 \mu\text{m}$ and $\max\{T_{\text{av}}\} \simeq -2.5 \text{ dB}$.

At this point, we should make an important observation: using FLG in order to achieve greater α_H , increases α_L by the same factor N which, according to (9), leads to

$$\tilde{L}_c(\alpha_H, \alpha_L) = \tilde{L}_c(\alpha_h, \alpha_\ell)/N, \quad (11a)$$

$$\max\{T_{\text{av}}(\alpha_H, \alpha_L)\} = \max\{T_{\text{av}}(\alpha_h, \alpha_\ell)\}. \quad (11b)$$

Furthermore, we argue that (11a) and (11b) stand not only for the usage of FLG but also when manipulating the way graphene is integrated in the waveguiding structure (e.g. position, waveguide type and dimensions). Assuming that the mode profile is only weakly perturbed by graphene in the high/low loss states then when seeking to maximize the overlap of the electric field with the graphene layers in order to attain a higher loss state at low μ_c , inevitably losses will increase by the same factor in the high μ_c regime. Hence, we would again reach (11) but with N representing the increase/decrease of the field overlap. Thus, for all graphene-like materials, whose low and high loss state cannot be independently manipulated there exists a lower boundary intrinsic to the material for the average insertion losses. Nevertheless, even though IL are intrinsic to the material choice, according to (11a) the length L_c of the photonic device is reduced by a factor of N which justifies the incorporation of FLG as well as the need for a judicious waveguide design.

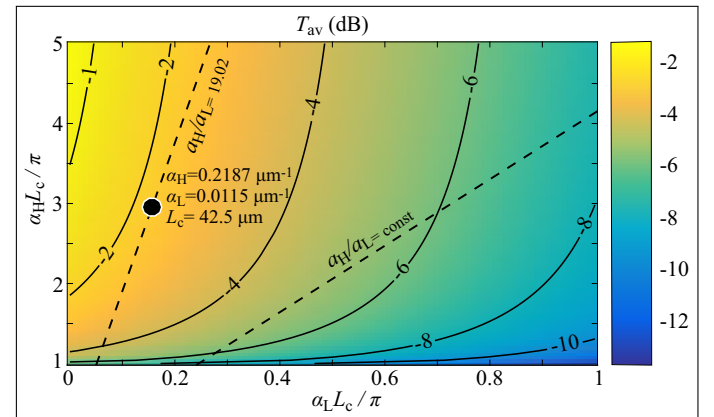


Fig. 5. Map of T_{av} in (dB) versus $\alpha_H L_c/k_0$ and $\alpha_L L_c/k_0$. The dashed lines correspond to the trajectory of a point with fixed α_H , α_L and variable L_c . A circle denotes the point that corresponds to the parameters used in this section. The maximum of the transmission is only observed when $\alpha_L \neq 0$.

We want to stress here that a realistic model of graphene's surface conductivity was taken into account, without neglecting losses [31] at high μ_c . The non-zero upper boundary of T_{av} is a direct consequence of $\alpha_L \neq 0$. A map of T_{av} versus $\alpha_H L_c$ and $\alpha_L L_c$ is plotted in Fig. 5. The optimal coupling length point of (9a) can be found along the dashed lines which mark the trajectory of a point with fixed α_H , α_L and variable L_c . These lines, which essentially are the locus of the points satisfying $\alpha_H/\alpha_L = \text{const}$, always intersect the same contour twice unless $\alpha_L = 0$, at which point they become vertical. Finally, another implication of graphene's small but not negligible losses for

$\mu_c > 0.4$ eV, is the choice of coating only one of the waveguides with graphene sheets, either monolayers or FLG sheets. If we had also considered the second waveguide to be lossy with loss coefficient α_L then not only $\Delta\alpha = \alpha_H - \alpha_L$ in (2) would decrease requiring a higher α_H to maintain the same operation point but also, more importantly, losses in the low loss state would double, hindering potential applications.

4. RESULTS AND DISCUSSION

Since the fundamentals of the switching operation were presented in detail in Section 2 and 3B, in the current section we present the transmission characteristics of such a photonic switch alongside insight of the physical system and materials involved, and we validate through simulations the conclusions that were drawn from the analytic expressions.

We employ a FEM method to numerically calculate the propagation constants of the supported eigenmodes of the coupled and uncoupled waveguides as well as calculate the coupling coefficient. Note that L_c is derived from the coupled waveguide system when both waveguides are considered lossless. The results from the FEM formulation are then passed on to the CMT equations of (1) which can be either numerically solved through a Runge-Kutta method or by employing the known analytic solution of a 2×2 system. We retain the waveguide dimensions reported at the start of Section 3 as they were already meticulously chosen for an excellent overlap of the TE mode with graphene.

Finally, using a separate waveguide-graphene scheme we exemplify polarization dependent switching based on graphene's anisotropy and the switching process described so far.

A. Photonic Switch

We start by calculating the normalized transmission and ER at the cross ($\mu_c = 0.48$ eV) and bar ($\mu_c = 0.2$ eV) state versus the coupling length L_c of the coupler. We consider FLG layers with $N = 3$. Note that L_c can be tuned without affecting the rest of the system by adjusting the gap between the waveguides. The normalized transmission is depicted in Fig. 6(a) where the simulated optimal coupling length is found at $39.22 \mu\text{m}$ (denoted with a diamond). Compared to the analytic calculation of $T_{av} = 0.5(T_{bar} + T_{cross})$ from (4), (7) and (9b), also shown in Fig. 6(a), there is a small deviation originating from the simplifying assumptions of the model used. Thereafter, calculated values of \tilde{L}_c will be implicitly assumed to have been extracted through simulation. Furthermore, we note that for a wide range of L_c values, T_{av} around the optimal point is almost constant [inset of Fig. 6(a)].

The dependence of the ER on L_c is plotted in Fig. 6(b) where 14 dB of ER at \tilde{L}_c is observed. In both states analytic expressions of the ER can be extracted from (5) and [40]:

$$ER_{bar} = \frac{\left[\alpha_H L_c + \sqrt{(\alpha_H L_c)^2 - \pi^2} \right]^2}{\pi^2}, \quad (12a)$$

$$ER_{cross} = \frac{\frac{\pi^2}{4\zeta^2} \sin^2(\zeta)}{\left[\cos(\zeta) + \frac{\sqrt{\pi^2 - 4\zeta^2}}{2\zeta} \sin(\zeta) \right]^2}, \quad (12b)$$

where $\zeta = 0.5\sqrt{\pi^2 - (\alpha_L L_c)^2}$. It is evident from (5) and (12) that ER is the product of interference solely in the cross state. Specifically, ER in the bar state depends on L_c (through $|\kappa|$) but

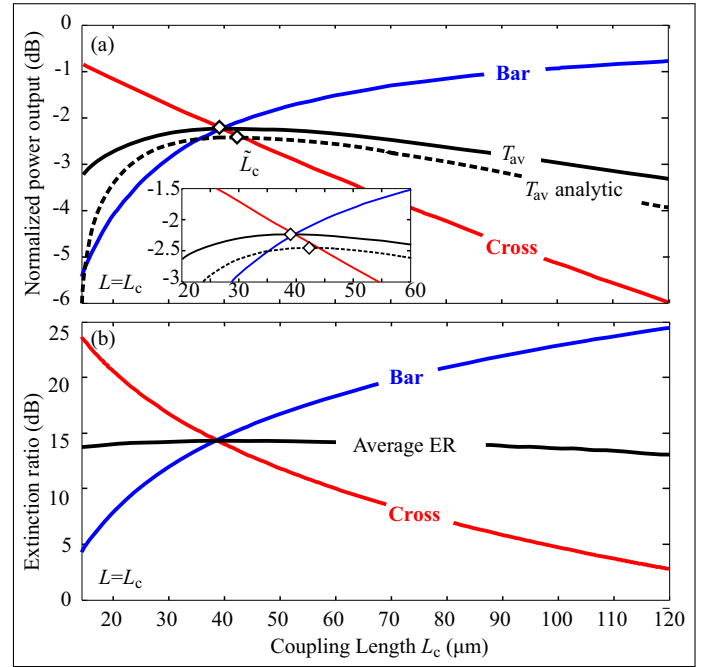


Fig. 6. (a) Normalized power transmission and (b) ER for a coupler of length $L = L_c$ for various values of L_c . Only excitation of the lossless waveguide is considered hence the cross (red solid line) and bar (blue solid line) output ports coincide with the lossy and lossless waveguides, respectively. A black solid or dashed line in (a) depicts the simulated or analytically predicted average losses $T_{av} = 0.5(T_{bar} + T_{cross})$ of (4) and (7), respectively. The optimal coupling length \tilde{L}_c of both analytic (9a) and simulated average losses is denoted with a diamond on the respective curve. A zoom-in around \tilde{L}_c is shown in the inset, where small dependence of T_{av} to L_c is observed. The average ER (black solid line) in (b) is observed to be almost independent of L_c near \tilde{L}_c .

it is otherwise independent of the propagation distance. Also note that the expressions in (12a) and (12b) are a function of $\alpha_H L_c = \alpha_H N L_c$ and $\alpha_L L_c = \alpha_L N L_c$, respectively, which suggests that the dependence of ER on L_c shown in Fig. 6(b) is actually on the product $N L_c$.

Consequently, according to Fig. 6, it is not mandatory for the system to be tuned to \tilde{L}_c exactly, allowing for a trade-off between IL and the footprint/ER of the switch. Interestingly the average ER as well as average IL between the two states are almost constant in the vicinity of \tilde{L}_c and thus the minimum length of the device can be set so that the bar state exhibits an acceptable level of both ER and IL.

We now present in Fig. 7 the evolution of the coupler's eigenvalues as a function of graphene's chemical potential. The EP and the subsequent near-coalescence of the eigenvalues are readily identified. Note that in Fig. 7(a) we elect to present the evolution of n_{eff} by artificially varying the real part of graphene's conductivity, in a linear manner, between the values $11.62 \mu\text{S}$ and $187.3 \mu\text{S}$ corresponding to 0.48 eV and 0.2 eV, respectively. This is done so as to render the transition from the EP easily discernible. It is understood that it is not possible to linearly vary graphene's conductivity in this fashion since the dependence of the conductivity on μ_c is given in Fig. 2. Finally, notice that the transition from the EP in Fig. 7(a) is not as sharp as in

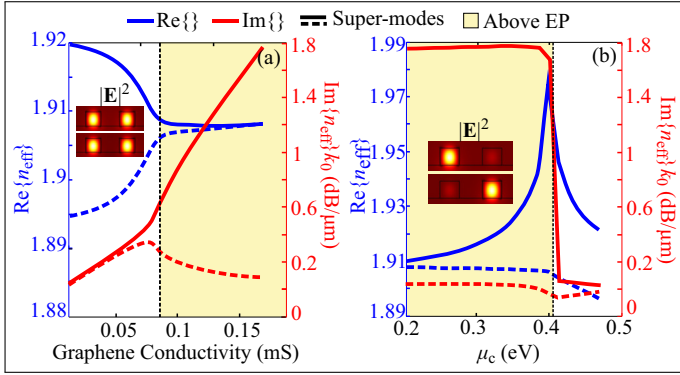


Fig. 7. Evolution of the real (blue) and imaginary (red) part of n_{eff} of the supported super-modes (solid/dashed) with respect to graphene's μ_c . In (a) only the real part of graphene's conductivity is varied, in an artificially linear manner, between the respective values at 0.48 eV and 0.2 eV so as to make the EP easily identifiable. The complete picture of the evolution versus the chemical potential is shown in (b). The insets show the field distribution of $|E|^2$ below (a) and above (b) the EP.

a perfectly gain/loss balanced PT-Symmetric system [41, 42] a feature which arises from the complex coupling coefficients of non-ideal systems.

The complete picture of the evolution of n_{eff} versus graphene's chemical potential is depicted in Fig. 7(b), where again we note the significance of biasing graphene away from the 0.4 eV point. Even though Fig. 7(b) is not a typical representation of the transition from an EP, all the salient points are still there: for low μ_c the imaginary part bifurcates whereas the real part is almost the same between the two modes. The reverse holds for high μ_c . For switching operation, the cross and bar states correspond to the maximum and minimum values of the chemical potential in the graphs shown.

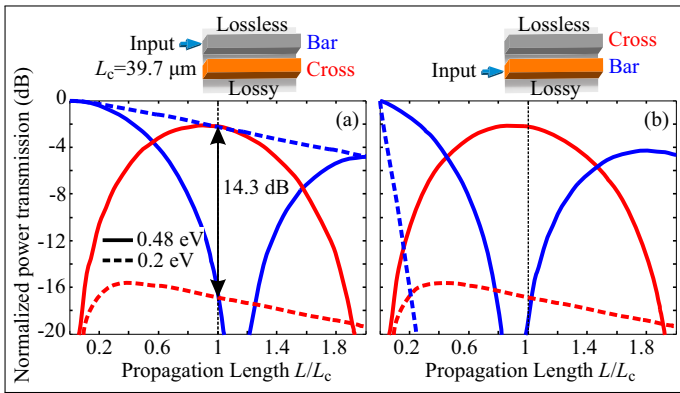


Fig. 8. Normalised power transmission for operation below (solid) and above (dashed) the EP and for excitation of both (a) the lossless and (b) lossy waveguide. The coupling length $L_c = 39.7 \mu\text{m}$ (440 nm gap) is very close to the optimal value $\bar{L}_c = 39.22 \mu\text{m}$. Bar and cross output is denoted with blue and red, respectively. Excitation of the lossy waveguide is not possible for switching operation due to detrimental IL (b), thus the device can only operate as a 1×2 switch. Note that cross curves in (a) and (b) are identical since the system is asymmetric but still reciprocal. Black arrows in (a) graphically show ER for excitation of the lossless waveguide.

The normalised power transmission in both states versus the propagation distance is plotted in Fig. 8 for excitation of both the lossless [Fig. 8(a)] and lossy [Fig. 8(b)] waveguide. We note that excitation of the lossy waveguide results into heavy losses, as predicted by (8), and thus is deemed impractical, which limits the switching functionality of our design to 1×2 . Comparison between Fig. 8(a) and 8(b) reveals that although the system is asymmetric (barely noticeable below the EP but very prevalent above it) reciprocity still holds, as the cross transmission is identical in both states, which was also analytically shown in (5). Finally, contrary to the cross state, in the bar state we note that ER is constant, e.g. the dashed lines in Fig. 8 are parallel [this can also be analytically inferred from (5) noting that the z dependence is eliminated]. The constant ER is a direct consequence of the EP transition and the vanishing of the high-loss super-mode after sufficient propagation distance.

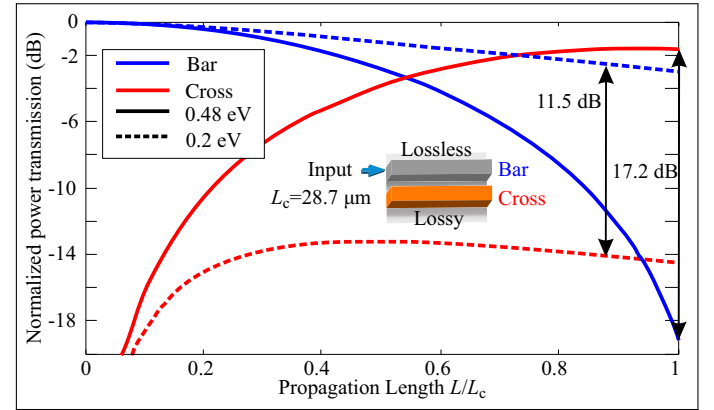


Fig. 9. Normalised power transmission for a coupler with $L_c = 28.7 \mu\text{m} \neq \bar{L}_c = 39.22 \mu\text{m}$. Blue and red lines denote bar and cross output, respectively, while solid and dashed lines reflect the μ_c value. Black arrows graphically show the ER in the bar and cross state.

So for excitation of the lossless waveguide and the adopted parameter values of μ_c , $L_c = 39.7 \mu\text{m}$ (440 nm gap) and propagation distance equal to the coupling length, IL and ER are found to be 2.2 dB and 14.3 dB, respectively, in both states, which is the best possible performance for the selection of materials in terms of IL and ER. Insofar the length of the device is concerned, the fact that bar output is not governed by interference of the super-modes can be exploited for applications requiring small footprint. As was mentioned previously, inspecting Fig. 6(a),(b) we deduce that we could decrease L_c below the optimal point with the trade-off of increasing losses and deteriorating ER in the bar state but decreasing losses and improving ER in the cross state. For example, if the limit of acceptable losses and ER is set at 3 dB and 10 dB, respectively, then the device length can be reduced to $28.7 \mu\text{m}$ (corresponding to a 390 nm gap) with 1.6 dB/3 dB IL and 17.2 dB/11.5 dB ER in the cross and bar state, respectively. The corresponding power transmission curves are shown in Fig. 9. A summary of IL and ER values for both of the cases discussed can be found in Table 1. Energy consumption for switching between the chosen chemical potential values can be estimated from (10) and the expression [43]: $W = C\Delta V^2/4$, where C is the capacitance of the graphene/alumina/graphene parallel plate capacitor and ΔV is the difference of the biasing voltage in the two states. The switching energy is roughly estimated to be 50 fJ.

Table 1. Aggregated values of IL and ER in the bar and cross state for $L = \tilde{L}_c = 39.7 \mu\text{m}$, $L = L_c = 28.7 \mu\text{m}$, and $L < L_c = 28.7 \mu\text{m}$.

	$L = 39.7 \mu\text{m}$		$L = 28.7 \mu\text{m}$	
Gap	440 nm		390 nm	
	Cross		Bar	
IL (dB)	2.2	2.2	1.6	3
ER (dB)	14.3	14.3	17.2	11.5

Finally, we verify that minimum IL are independent of graphene position and FLG layers, as predicted by (11b). We numerically calculate the propagation constants of the first TE eigenmode in the uncoupled waveguides for various values of N . We then employ the CMT equations of (1) and for each value of N we find the coupling length which leads to the least amount of losses for propagation distance equal to the coupling length. The results are shown in Fig. 10(a). Next, we perform the same procedure but instead of varying the number of graphene sheets ($N = 3$) we alter the vertical position of the graphene/alumina/graphene stack in the waveguide. The position is measured from the substrate (0 nm) to the top of the silicon waveguide (280 nm). In this scenario we define N' as the increase/decrease in the field overlap with graphene and calculate it as $\alpha_H/\alpha_{h'}$, where α_h is the loss coefficient at 280 nm. Results are presented in Fig. 10(b). The dashed black line stands for the series $1/N$ or $1/N'$ which is what (11a) predicts concerning the evolution of the optimal coupling length point. It is evident that there is excellent agreement between numerical and analytic results, highlighting that maximum average transmission is truly independent of graphene position or graphene layers and it only depends on the α_L/α_H ratio that graphene can provide [see (9)].

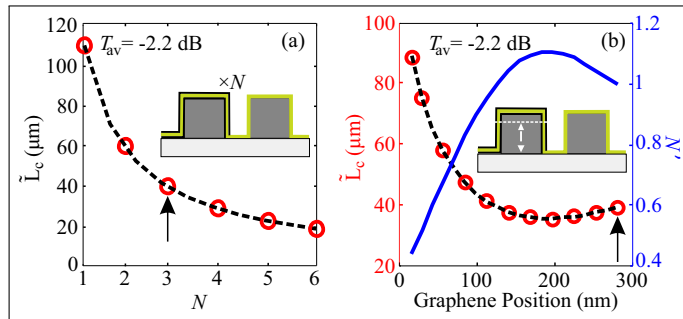


Fig. 10. Optimal coupling length \tilde{L}_c (red circles) versus (a) the number N of graphene layers in the FLG (inset) and (b) versus (tri-layer) graphene's position, measured from the substrate (inset). A blue solid line in (b) shows N' versus graphene position, where N' is calculated as $\alpha_{H,L}/\alpha_{h,l}$ and translates to the increase/decrease in the field overlap with graphene. Note that $N = 3$ in (a) corresponds to $N' = 1$ in (b). Black arrows show the points corresponding to the scenario of Fig. 8. The black dashed curve in both (a) and (b) verifies the expected $1/N$ or $1/N'$ dependence of \tilde{L}_c . T_{av} is constant in both scenarios and equal to -2.2 dB.

B. Polarisation dependent switching

In this final section, we exploit the switching capabilities of a passive PT-Symmetric coupler and the inherent anisotropy of graphene to theoretically design a polarization dependent switch. Graphene due to its 2D nature, interacts with electromagnetic radiation polarised parallel to its surface, thus it provides a way of differentiating the losses experienced by polarizations whose dominant electric field is polarized perpendicular or parallel to the graphene sheet, such as the TE (dominant E_x) and TM (dominant E_y) modes in a photonic waveguide.

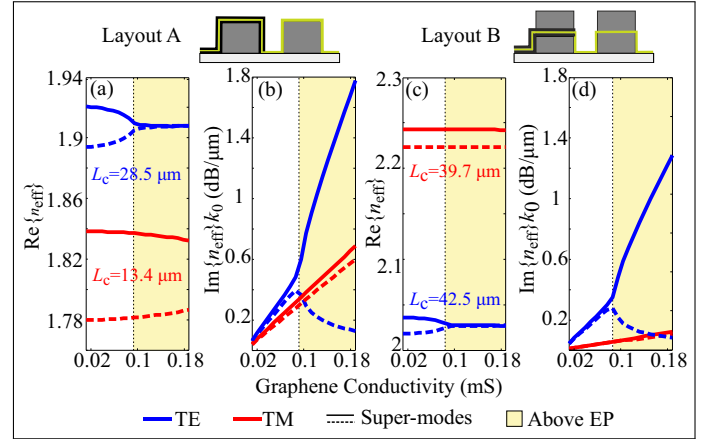


Fig. 11. Evolution of the n_{eff} of the TE (blue) and TM (red) supported super-modes (solid/dashed). (a),(b) correspond to the waveguide layout A, identical to that of Section A and (d),(c) to the waveguide layout B examined in Section B. The cross-sections of the waveguide geometries are also shown above the respective graphs. In all cases, only the real part of graphene's conductivity is varied (artificially in a linear manner) between its value at 0.48 eV and 0.2 eV, which better illustrate the coalescence of the eigenmodes. Comparison between (a),(b) and (c),(d) shows that in the latter case the TM mode does not experience an EP while also exhibiting low losses.

Polarisation dependent switching based on passive PT-Symmetry, according to (2), requires that either losses or coupling strength are adequately differentiated with respect to polarisation. In the design examined in Section A, TE and TM polarizations exhibit distinct EPs due to their different coupling lengths, e.g. a gap of 390 nm leads to $28.7 \mu\text{m}$ and $13.4 \mu\text{m}$ for the TE/TM mode, respectively. Consequently, since the TM mode has a much lower L_c , it does not reach the EP for $\mu_c = 0.2 \text{ eV}$ but simply experiences high propagation losses, as depicted in Fig. 11(a),(b). The high TM losses are attributed to the fact that the coating of graphene around the waveguide effectively mitigates graphene's anisotropy providing almost equal overlap to both polarizations [see Fig. 4(d)-(f)].

Thus the TE/TM modes need to have the same L_c , so that they both exit the coupler at the same propagation length, but drastically different overlap with graphene, so that the mode that does not experience an EP does not also suffer from severe losses. Note that the mode that is not switched could potentially have a lower coupling length as long as it is an integer sub-multiple. We elect here to present a scenario of equal coupling lengths in order to highlight graphene anisotropy.

To achieve this, the silicon waveguide dimensions are altered to 310 nm wide and 390 nm tall and the gap is set to 400 nm leading to a coupling length of $42.5 \mu\text{m}$ and $39.7 \mu\text{m}$

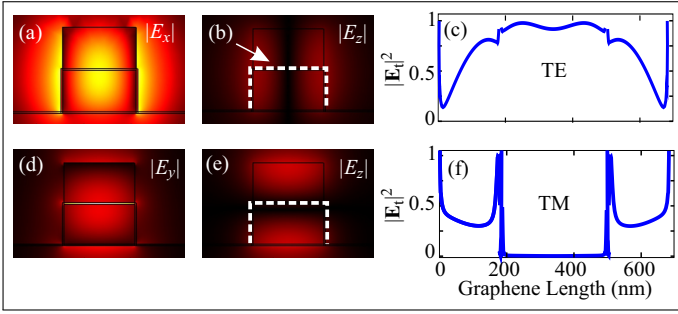


Fig. 12. Field distributions of the norm of the electric field components of the first (a),(b) TE and (d),(e) TM modes, respectively, supported by the waveguide layout of Section B. A white dashed line highlights the graphene curve on which the norm of the tangential electric field E_t is calculated and depicted in (c) for the TE mode and (f) for the TM mode. Graphene coating on the side of the waveguide, contrary to Fig. 4(c), is less significant to TE mode losses. Graphene placed in the middle of the waveguide exhibits very weak overlap with the TM mode both because of the y polarization (d) and due to the absence of the E_z component (e).

for the TE and TM mode, respectively. The suggested dimensions are chosen so as to achieve almost equal coupling length and enable efficient polarization dependent switching but are in no way optimized. Following the change of dimensions, the graphene/alumina/graphene stack is placed through the middle of the silicon area as depicted in the inset marked as layout B in Fig. 11. Notice that there is graphene coating only on one side of the waveguide. The absence of this graphene side-coating further limits the TM's mode overlap with graphene since it strongly contributed to the TM losses but had only mediocre overlap with the TE mode. The field overlap with graphene for the case of the fully coated waveguides is plotted in Fig. 12(a)-(c) for the TE mode and 12(d)-(f) for the TM mode showing that the side-coating is much more significant to the TM mode than the TE mode. Comparing Fig. 11(a),(b) to Fig. 11(c),(d) reveals that the TE/TM super-modes of the new waveguide layout have acquired the desired relation between them for polarization dependent switching.

The power transmission for light injection in the lossless waveguide is presented in Fig. 13 for the TE and TM mode, respectively. The TE mode behaviour is similar to Fig. 9, with operation above and below the EP denoting a bar and a cross state. On the other hand the TM mode is in the cross state regardless of graphene's biasing conditions (i.e. a conventional lossy photonic coupler). Thus by tuning graphene's μ_c to 0.48 eV or 0.2 eV, we dynamically control whether the TE and TM mode are spatially separated in the output of the coupler. For a coupler length equal to the TM mode's coupling length of $\sim 40 \mu\text{m}$ (depicted with a vertical black line in Fig. 13) an overview of the operation with the respective IL and ER is presented in Table 2.

5. CONCLUSIONS

We have presented a comprehensive analytical and numerical study of the operation of a passive and linear photonic coupler under the influence of a loss-induced EP through this shown that loss-manipulating effects in graphene can be exploited to effectively control light. By varying the loss coefficients of the supported photonic modes we analytically derived all the salient

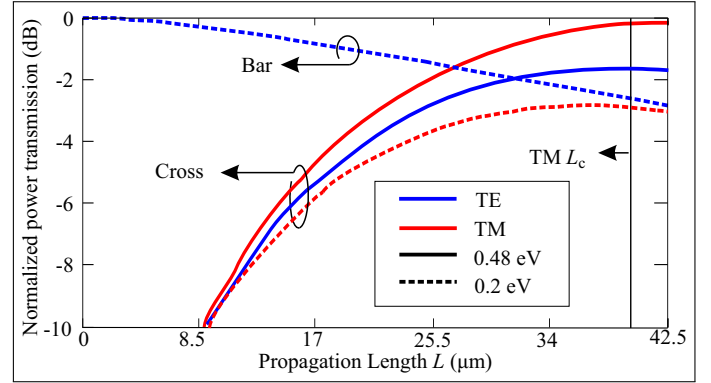


Fig. 13. Normalized power transmission for the TE (blue) and TM (red) mode. Solid/dashed lines correspond to μ_c 0.48 eV and 0.2 eV, respectively. The coupler output ports are set at $L = 39.7 \mu\text{m}$ which coincides with the TM L_c (vertical black line). Only the TE mode is able to be switched to the bar state, whereas the TM mode is always in the cross state.

Table 2. Overview of the calculated IL/ER of the polarization dependent switch for $L = L_c = 39.7 \mu\text{m}$.

μ_c	TE		TM			
	State	IL	ER	State	IL	ER
0.48 eV	Cross	1.7 dB	12.0 dB	Cross	0.2 dB	>20 dB
0.2 eV	Bar	2.6 dB	11.1 dB	Cross	3.2 dB	10.2 dB

features of a linear passive PT-Symmetric 1×2 photonic switch (existence of an EP, coalescence of eigenmodes, reciprocity, IL and ER) and extracted a lower boundary for the IL of such a device. Although the equations were formulated based on a photonic coupler of two straight waveguides, the complete analysis and conclusions can be readily extended to other coupled photonic elements such as coupled resonators. Graphene and FLG were elected as the material of choice for the practical implementation of the passive PT-Symmetry dynamics, which was based on graphene's tunable surface conductivity. We established proper biasing conditions for graphene's chemical potential, in order to ensure that operation is based on the existence of an EP, and theoretically investigated a silicon photonic coupler enhanced with graphene. Through this investigation we confirmed all the analytic conclusions drawn and assessed the transmission characteristics of the proposed passive and linear electro-optic 1×2 switch based on IL (2.2 dB), ER (14.3 dB) and footprint ($39 \mu\text{m}$). Due to the distinct interference/non-interference based operation at the cross/bar state, respectively, by allowing for higher IL (<3 dB) in the bar state and lower ER (>10 dB) in the cross state, the length of the device was lowered down to $29 \mu\text{m}$. Finally, by engineering the waveguide dimensions and graphene placement we theoretically showed a polarization dependent photonic switch based on EP dynamics and the anisotropic property of graphene's surface conductivity.

This research is implemented through IKY scholarships programme and co-financed by the European Union (European Social Fund - ESF) and Greek national funds through the action entitled "Scholarships program for postgraduates studies -2nd Study Cycle", in the framework of the Operational Programme

"Human Resources Development Program, Education and Life-long Learning" of the National Strategic Reference Framework (NSRF) 2014-2020.

REFERENCES

- W. D. Heiss, "The physics of exceptional points," *J. Phys. A: Math. Theor.* **45**, 444016 (2012).
- J. Doppler, A. A. Mailybaev, J. Böhm, U. Kuhl, A. Girschik, F. Libisch, T. J. Milburn, P. Rabl, N. Moiseyev, and S. Rotter, "Dynamically encircling an exceptional point for asymmetric mode switching," *Nature* **537**, 76–79 (2016).
- F. Fotsa-Ngafo, S. B. Tabeu, S. Tagouegni, and A. Kenfack-Jiotsa, "Thresholdless characterization in space and time reflection symmetry electronic dimers," *J. Opt. Soc. Am. B* **34**, 658–667 (2017).
- C. M. Bender and S. Boettcher, "Real spectra in non-hermitian hamiltonians having \mathcal{PT} symmetry," *Phys. Rev. Lett.* **80**, 5243–5246 (1998).
- K. G. Makris, R. El-Ganainy, D. N. Christodoulides, and Z. H. Mussli-mani, "Beam dynamics in \mathcal{PT} symmetric optical lattices," *Phys. Rev. Lett.* **100**, 103904 (2008).
- C. E. Rüter, K. G. Makris, R. El-Ganainy, D. N. Christodoulides, M. Segev, and D. Kip, "Observation of parity-time symmetry in optics," *Nat. Phys.* **6**, 192–195 (2010).
- F. Nazari, M. Nazari, and M. K. Moravvej-Farshi, "A 2×2 spatial optical switch based on \mathcal{PT} -symmetry," *Opt. Lett.* **36**, 4368–4370 (2011).
- A. Lupu, H. Benisty, and A. Degiron, "Switching using \mathcal{PT} symmetry in plasmonic systems: positive role of the losses," *Opt. Express* **21**, 21651–21668 (2013).
- A. Lupu, H. Benisty, and A. Degiron, "Using optical \mathcal{PT} -symmetry for switching applications," *Photonics Nanostructures - Fundamentals Appl.* **12**, 305 – 311 (2014).
- B. Baum, H. Alaeian, and J. Dionne, "A parity-time symmetric coherent plasmonic absorber-amplifier," *J. Appl. Phys.* **117**, 063106 (2015).
- H. Benisty, A. Lupu, and A. Degiron, "Transverse periodic \mathcal{PT} symmetry for modal demultiplexing in optical waveguides," *Phys. Rev. A* **91**, 053825 (2015).
- L. Feng, Z. J. Wong, R. Ma, Y. Wang, and X. Zhang, "Single-mode laser by parity-time symmetry breaking," *Science* **346**, 972–975 (2014).
- A. Regensburger, C. Bersch, M. Miri, G. Onishchukov, D. N. Christodoulides, and U. Peschel, "Parity-time synthetic photonic lattices," *Nature* **488**, 167–171 (2012).
- L. Feng, Y. Xu, W. S. Fegadolli, M. Lu, J. E. B. Oliveira, V. R. Almeida, Y. Chen, and A. Scherer, "Experimental demonstration of a unidirectional reflectionless parity-time metamaterial at optical frequencies," *Nat. Mater.* **12**, 108–113 (2013).
- A. Laha and S. Ghosh, "Connected hidden singularities and toward successive state flipping in degenerate optical microcavities," *J. Opt. Soc. Am. B* **34**, 238–244 (2017).
- B. Peng, C. K. Özdemir, F. Lei, F. Monifi, M. Gianfreda, G. L. Long, S. Fan, F. Nori, C. M. Bender, and L. Yang, "Parity-time-symmetric whispering-gallery microcavities," *Nat. Phys.* **10**, 394–398 (2014).
- A. Guo, G. J. Salamo, D. Duchesne, R. Morandotti, M. Volatier-Ravat, V. Aimez, G. A. Siviloglou, and D. N. Christodoulides, "Observation of \mathcal{PT} -symmetry breaking in complex optical potentials," *Phys. Rev. Lett.* **103**, 093902 (2009).
- M. Liu, X. Yin, E. Ullin-Avila, B. Geng, T. Zentgraf, L. Ju, F. Wang, and X. Zhang, "A graphene-based broadband optical modulator," *Nature* **474**, 64–67 (2011).
- T. Cassese, M. A. Giambra, V. Soriano, G. D. Angelis, M. Midrio, M. Pantouvaki, J. V. Campenhout, I. Asselberghs, C. Huyghebaert, A. D'Errico, and M. Romagnoli, "Capacitive actuation and switching of add-drop graphene-silicon micro-ring filters," *Photon. Res.* **5**, 762–766 (2017).
- Q. Bao, H. Zhang, B. Wang, Z. Ni, C. H. Y. X. Lim, Y. Wang, D. Y. Tang, and K. P. Loh, "Broadband graphene polarizer," *Nat. Photonics* **5**, 411–415 (2011).
- R. El-Ganainy, K. G. Makris, D. N. Christodoulides, and Z. H. Mussli-mani, "Theory of coupled optical \mathcal{PT} -symmetric structures," *Opt. Lett.* **32**, 2632–2634 (2007).
- Y. Li, X. Guo, L. Chen, C. Xu, J. Yang, X. Jiang, and M. Wang, "Coupled mode theory under the parity-time symmetry frame," *J. Light. Technol.* **31**, 2477–2481 (2013).
- A. W. Snyder and J. D. Love, *Optical Waveguide Theory* (Chapman and Hall, U.S.A., 1983).
- Z. Zheng, Z. Bo, and Z. Li-Juan, "Analytical study on propagation dynamics of optical beam in parity-time symmetric optical couplers," *Commun. Theor. Phys.* **63**, 406 (2015).
- M. Liu, X. Yin, and X. Zhang, "Double-layer graphene optical modulator," *Nano Lett.* **12**, 1482–1485 (2012).
- V. Soriano, M. Midrio, and M. Romagnoli, "Design optimization of single and double layer graphene phase modulators in soi," *Opt. Express* **23**, 6478–6490 (2015).
- K. S. Novoselov, A. K. Geim, S. V. Morozov, D. Jiang, M. I. Katsnelson, I. V. Grigorieva, S. V. Dubonos, and A. A. Firsov, "Two-dimensional gas of massless dirac fermions in graphene," *Nature* **438**, 197 EP – (2005).
- L. A. Falkovsky, "Optical properties of graphene," *J. Physics: Conf. Ser.* **129** (2008).
- A. Y. Nikitin, F. Guinea, F. J. Garcia-Vidal, and L. Martin-Moreno, "Edge and waveguide terahertz surface plasmon modes in graphene microribbons," *Phys. Rev. B - Condens. Matter Mater. Phys.* **84** (2011).
- X. Lin, R. Li, F. Gao, E. Li, X. Zhang, B. Zhang, and H. Chen, "Loss induced amplification of graphene plasmons," *Opt. Lett.* **41**, 681–684 (2016).
- A. Locatelli, A.-D. Capobianco, M. Midrio, S. Boscolo, and C. D. Angelis, "Graphene-assisted control of coupling between optical waveguides," *Opt. Express* **20**, 28479–28484 (2012).
- D. Chatzidimitriou, A. Ptilakis, and E. E. Kriezis, "Rigorous calculation of nonlinear parameters in graphene-comprising waveguides," *J. Appl. Phys.* **118** (2015).
- A. Grüneis, C. Attaccalite, L. Wirtz, H. Shiozawa, R. Saito, T. Pichler, and A. Rubio, "Tight-binding description of the quasiparticle dispersion of graphite and few-layer graphene," *Phys. Rev. B - Condens. Matter Mater. Phys.* **78** (2008).
- K. F. Mak, J. Shan, and T. F. Heinz, "Electronic structure of few-layer graphene: Experimental demonstration of strong dependence on stacking sequence," *Phys. Rev. Lett.* **104** (2010).
- Y. Wang, Z. Ni, L. Liu, Y. Liu, C. Cong, T. Yu, X. Wang, D. Shen, and Z. Shen, "Stacking-dependent optical conductivity of bilayer graphene," *ACS Nano* **4**, 4074–4080 (2010).
- C. Casiraghi, A. Hartschuh, E. Lidorikis, H. Qian, H. Harutyunyan, T. Gokun, K. S. Novoselov, and A. C. Ferrari, "Rayleigh imaging of graphene and graphene layers," *Nano Lett.* **7**, 2711–2717 (2007).
- R. R. Nair, P. Blake, A. N. Grigorenko, K. S. Novoselov, T. J. Booth, T. Stauber, N. M. R. Peres, and A. K. Geim, "Fine structure constant defines visual transparency of graphene," *Science* **320**, 1308–1308 (2008).
- Z. Rashidian, Y. V. Bludov, R. M. Ribeiro, N. M. R. Peres, and M. I. Vasilevskiy, "Optical conductivity of aba stacked graphene trilayer: mid-ir resonance due to band nesting," *J. Physics: Condens. Matter* **26**, 395301 (2014).
- K. Sugawara, N. Yamamura, K. Matsuda, W. Norimatsu, M. Kusunoki, T. Sato, and T. Takahashi, "Selective fabrication of free-standing aba and abc trilayer graphene with/without dirac-cone energy bands," *Npg Asia Mater.* **10**, e466 EP – (2018).
- H. A. Haus, *Waves and Fields in Optoelectronics* (Prentice-Hall, New Jersey, 1984).
- H. Benisty, C. Yan, A. Degiron, and A. Lupu, "Healing near- \mathcal{PT} -symmetric structures to restore their characteristic singularities: Analysis and examples," *J. Light. Technol.* **30**, 2675–2683 (2012).
- N. B. Nguyen, S. A. Maier, M. Hong, and R. F. Oulton, "Recovering parity-time symmetry in highly dispersive coupled optical waveguides," *New J. Phys.* **18**, 125012 (2016).
- D. A. B. Miller, "Energy consumption in optical modulators for interconnects," *Opt. Express* **20**, A293–A308 (2012).